Edinburgh Research Explorer

Demographics of the M-star Multiple Population in the Orion Nebula Cluster

Demographics of the M-star Multiple Population in the Orion Nebula Cluster

Matthew De Furio [ORCID],[1] Christopher Liu,[1] Michael R. Meyer,[1] Megan Reiter,[2] Adam Kraus,[3] Trent Dupuy,[4] and John Monnier[1]

[1]*Department of Astronomy, University of Michigan, Ann Arbor, MI 48109, USA*
[2]*Rice University, Houston, TX*
[3]*Department of Astronomy, University of Texas at Austin, Austin, TX 78712, USA*
[4]*Institute for Astronomy, University of Edinburgh, Royal Observatory, Blackford Hill, Edinburgh, EH9 3HJ, UK*

ABSTRACT

We present updated results constraining multiplicity demographics for the stellar population of the Orion Nebula Cluster (ONC, a high-mass, high-density star-forming region), across primary masses 0.08-0.7$M_\odot$. Our study utilizes archival Hubble Space Telescope data obtained with the Advanced Camera for Surveys using multiple filters (GO-10246). Previous multiplicity surveys in low-mass, low-density associations like Taurus identify an excess of companions to low-mass stars roughly twice that of the Galactic field and find the mass ratio distribution consistent with the field. Previously, we found the companion frequency to low-mass stars in the ONC is consistent with the Galactic field over mass ratios=0.6-1.0 and projected separations=30-160au, without placing constraints on the mass ratio distribution. In this study, we investigate the companion population of the ONC with a double point-spread function (PSF) fitting algorithm sensitive to separations larger than 10au (0.025") using empirical PSF models. We identified 44 companions (14 new), and with a Bayesian analysis, estimate the companion frequency to low-mass stars in the ONC =$0.13^{+0.05}_{-0.03}$ and the power law fit index to the mass ratio distribution =$2.08^{+1.03}_{-0.85}$ over all mass ratios and projected separations of 10-200au. We find the companion frequency in the ONC is consistent with the Galactic field population, likely from high transient stellar density states, and a probability of 0.002 that it is consistent with that of Taurus. We also find the ONC mass ratio distribution is consistent with the field and Taurus, potentially indicative of its primordial nature, a direct outcome of the star formation process.

Keywords: star formation, low-mass stars, multiplicity, star-forming regions

1. INTRODUCTION

Stellar multiple systems are a frequent outcome of star formation, and most stars form in clusters or associations with initial density much higher than the disk of the Milky Way. They are thought to be created through two dominant mechanisms, turbulent fragmentation (Goodwin et al. 2004; Offner et al. 2010) and disk fragmentation (Adams et al. 1989; Bonnell & Bate 1994; Kratter et al. 2008). Their properties (e.g. separation, mass ratio ($m_{companion}/m_{primary}$), and eccentricity) can be altered by various processes. The mass ratio can increase due to an inwardly migrating companion

Corresponding author: Matthew De Furio
defurio@umich.edu

preferentially accreting material from the circumstellar disk (Mazeh et al. 1992; Kroupa 1995a; Bate & Bonnell 1997; Bate 2000). Wide companions can migrate to closer separations through interactions with infalling gas from the protostellar cloud or circumstellar disk (Bate et al. 2002, 2003; Offner et al. 2010; Bate 2012). Other processes, like dynamical interactions between a multiple system and other cluster members, can even cause the complete dissolution of the multiple system (Kroupa et al. 2001).

Previous multiplicity surveys in the Galactic field have characterized the companion population as a function of primary mass (Duchêne & Kraus 2013; Offner et al. 2022). They find a separation distribution well-fitted with a log-normal where the mean separation appears to increase with primary mass: 6 au for very-low mass star and brown dwarf primaries (Reid et al. 2006), 20 au

for stellar M-type primaries (Janson et al. 2012; Winters et al. 2019), and 50 au for solar-type primaries (Raghavan et al. 2010).

Multiplicity surveys in young, nearby associations find an excess of companions to low-mass primary stars relative to the Galactic field (Ghez et al. 1993; Leinert et al. 1993; Reipurth & Zinnecker 1993; Simon et al. 1995; Brandner et al. 1996; Ghez et al. 1997). One such survey in the Taurus-Auriga dark cloud found a companion frequency of $0.79^{+0.12}_{-0.11}$ over all mass ratios and for separations of 3-5000 au for stars with primary masses of 0.25 - 0.7 $M_\odot$, roughly twice that of the Galactic field (Kraus et al. 2011). In our recent survey of the M-star multiple population in the Orion Nebula Cluster (ONC), we found a companion frequency of $0.08^{+0.04}_{-0.02}$ over mass ratios of 0.6 - 1.0 and separations of 30 - 160 au, consistent with the low-mass Galactic field population over the same parameter space (De Furio et al. 2019), a result supported by Strampelli et al. (2020). Importantly, these star-forming regions have disparate present-day stellar number densities, 1-10 pc^{-3} in Taurus (Luhman et al. 2009), and $10^{3.5-4.5}$ pc^{-3} in the ONC (Hillenbrand & Hartmann 1998; Marks & Kroupa 2012) while also thought to have experienced different densities throughout their lifetimes (Parker 2014).

In De Furio et al. (2019), we estimated the companion frequency in the ONC over specific mass ratios and separations by identifying companions using a double point-spread function (PSF) fitting routine with empirical PSF models (Anderson & King 2006). However, we were unable to place constraints on the mass ratio and orbital separation distributions due to the low number of detections. This was in part because we analyzed archival Hubble Space Telescope (HST) data from the Advanced Camera for Surveys (ACS) from the HST Treasury Program of the ONC (PID: 10246, Robberto et al. 2013) in only one filter (F555W). This limitation reduced the sample size of our survey due to severe saturation in long exposures. We updated our analysis routine to be sensitive to companions down to separations of 0.025" (De Furio et al. 2022), a region of parameter space in the ONC only explored for a handful of low-mass stars by Duchêne et al. (2018). It is necessary to probe this parameter space given the distance to the ONC (400 pc, Großschedl et al. 2018) because companions to M-type primary stars are commonly found around separations of 20 au in the Galactic field.

An expanded multiplicity survey with all available HST/ACS data is necessary to increase the sample size of the survey, identify more multiple systems, and derive specific functional forms of the companion population in terms of mass ratio and separation. As low-mass M-

type stars dominate the stellar population in terms of number and mass, placing constraints on its companion population in the ONC is crucial to understanding the dominant mechanisms of stellar multiple formation and identifying the impact of dynamics on multiple evolution.

In Section 2, we describe the data, the expanded ONC sample, and our method to detect companions. In Section 3, we present our companion detections and characterization of the companion population. In Section 4, we compare our results to those of the Galactic field and Taurus. In Section 5, we summarize our conclusions.

2. METHODS

In order to identify companions to our sample of stars in the ONC, we first applied the double-PSF fitting technique described in De Furio et al. (2019), hereafter Paper I. Then, we implemented the updated analysis, as described in De Furio et al. (2022) hereafter Paper II, in order to identify fainter and/or closer companions. We used data from all five ACS filters used in the HST Treasury Program of the ONC (F435W, F555W, F658N, F775W, and F850LP) to identify companions to a target list described in Sec. 2.3. This, combined with a Bayesian analysis of our results (described in Sec. 4), increased the sample size by a factor of three compared to the single filter, frequentist approach of Paper I.

2.1. *The Data*

We downloaded archival HST data taken with ACS on the Wide Field Camera (WFC) from GO program 10246 (PI: M. Robberto Robberto et al. 2013). The data analyzed in this paper were obtained from the Mikulski Archive for Space Telescopes (MAST) at the Space Telescope Science Institute, and can be accessed via DOI. This program captured a large mosaic of the ONC, covering 627 arcminutes, with four broadband filters and one narrow band filter: F435W, F555W, F658N, F775W, and F850LP. Each of the 104 pointings had an integration time of 420s, 385s, 340s, 385s, and 385s respectively and a field of view of 202" x 200", with no dithering or CR-SPLITing. The plate scale of ACS/WFC is 0.05"/pixel, undersampled across the visible spectrum (e.g. $\lambda/D = 0.037$" for F435W). We used empirical PSFs to fit the data and accurately estimate the centroid of the primary PSF and any potential companion. We use the _flt data products from the HST pipeline, which have been bias-subtracted and flat-fielded. These are the images specified by Anderson & King (2006), hereafter AK06, for which the empirical PSFs apply. Within these long exposures, many images suffered from severe saturation which prevented us from

performing PSF-fitting to many known members. In Paper II, we showed that a 0.2 $M_\odot$ star is at the saturation limit in the F435W exposures (as is a ~ 0.55 $M_\odot$ star with $A_v = 2$), and a 0.03 $M_\odot$ object is at the saturation limit in the F850LP exposures (0.07 $M_\odot$ with $A_v = 3$). A more thorough description of the data can be found in Robberto et al. (2013).

2.2. *Double-PSF Fitting with Empirical PSFs*

We have described the double-PSF fitting process and the PSF models in Paper I, but provide a summary below. The empirical PSFs were constructed by AK06 specifically for the ACS/WFC in multiple filters using real data across both detectors. For each filter, they created a library of 90 PSFs, spread across both chips of the ACS, 4x super-sampled over a radius of 12.5 ACS/WFC pixels. All filters used had a specific PSF library, except for F555W, and instead we use the F606W PSF library, as the differences are negligible (J. Anderson, private communication). To construct a PSF at a given location on the detector, we identify the four nearest empirical PSFs. For each pixel within a 21x21 stamp centered on the target, we perform a bi-cubic interpolation of each of the four empirical PSFs based on the distance of that pixel to the center of the stamp and linearly interpolate those resulting four pixel values based on the proximity of each empirical PSF to the location of the target on the detector. This results in a detector-sampled PSF. AK06 also provide a function to perturb the PSF models based on the brightest PSFs within a given image to account for changes in focus and pointing instability. We applied the perturbation to the PSF library of each filter for each image, effectively generating slightly different PSFs for each observation.

In order to identify companions, we fit a double-PSF model (constructed from two detector-sampled PSFs) to a postage stamp of 21x21 pixels centered around a given target that has already had the mean background subtracted from an inner and outer annulus of 10 and 15 pixels, respectively. Our model has six parameters: x and y center of the primary, combined magnitude of the system, separation between the centers of the primary and secondary, position angle corresponding to the center of the secondary, and the difference in magnitude (Δmag) between the primary and secondary.

We use the downhill simplex routine (AMOEBA) in IDL (Press et al. 2007) to sample the parameter space and identify the best-fit six parameter model by minimizing the χ^2_ν test statistic. This process is repeated 200 times to adequately sample the parameter space and then derive errors for each variable. Although we are deriving the best-fit double-PSF model to each input

postage stamp, this does not mean that each fit is identifying a companion. In Sec. 2.4, we summarize how we differentiate between a true detection of a companion and a false positive fit.

2.3. *The Sample*

The target list was constructed from Da Rio et al. (2016). They used the Sloan 2.5m telescope and the APOGEE spectrograph (R $\sim$ 22,500) to obtain multi-object spectroscopy in the H-band of roughly 2700 sources in the ONC. With these data, they were able to estimate the T_{eff}, log g, $v \sin i$, and extinction.

We searched through each of the 104 images in the five filters and identified which of the members exist within the data. Then, we determined whether or not the central pixel value was above 55,000 counts, to exclude sources affected by saturation (AK06). Finally, we ran the double-PSF fitting algorithm on each target in each image in which it was detected. Following the prescription of Paper I and II, we set a chi squared threshold to indicate a reasonable fit where the data are likely described by the six-parameter double-PSF model, here a p-value of 0.1, $\chi^2_\nu = 1.774$. Nebulosity is the key factor for poor fits within these data as spatially variable extended emission is not factored into the model and results in high χ^2_ν values. This process left us with 198 sources in F435W, 143 sources in F555W, 226 sources in F658N, 11 sources in F775W, and 5 sources in F850LP. Source counts are very low in F775W and F850LP due to saturation. In total, we have 276 unique sources throughout all filters, and 245 sources among the broadband filters with which we can estimate masses of the multiple systems.

2.4. *Companion Identification*

In Paper II, we thoroughly described the process by which we determine whether any given double-PSF fit is truly detecting a companion or is a false positive result. We summarize this process below.

We generated 1000 artificial single stars for each of the various S/N values (15 - 130) and within each filter using the empirical PSF model libraries of AK06 across the detector with added Poisson noise. Then, we ran the double-PSF fitting routine on each of these artificial single stars. For every individual single star, we take each iteration from the fitting process (a six parameter binary model with a χ^2_ν test statistic) and evaluate its chi squared probability P(χ^2). We then defined a wide region of interest in the separation and Δmag parameter space where the code is likely to fit a binary model regardless of the true astrophysical scene. This extends from 0 - 10 pixels in separation and 0 - 10 magnitudes

in Δmag which encompasses the entirety of our search radius and continues beyond the background noise level. This space was split into bins of 0.1 pixels and 0.1 magnitudes within which we select the best-fit, highest $P(\chi_\nu^2)$, model to each artificial single. This process results in a probability distribution that describes the fit to each artificial single star. We repeat this process for all artificial singles, and the resulting distributions are added giving a total probability distribution of fits to artificial singles of a given S/N and filter.

These distributions represent the parameter space in which the code will converge around single stars, i.e. a false positive fit. We sum the distribution vertically (in Δmag space) for each separation bin (0.1 pixels) which describes the Δmag where a certain percentage of the known false positive fits will lie below. We can then take the normalized distribution of any binary fit to real data and multiply it by these false positive maps, based on the filter and S/N of the source, and sum the resulting distribution to arrive at the probability that a given binary fit to data is a false positive. Based on our sample size, we define a false positive probability $< 0.1\%$ as indicative of a true binary detection, see Fig. 1.
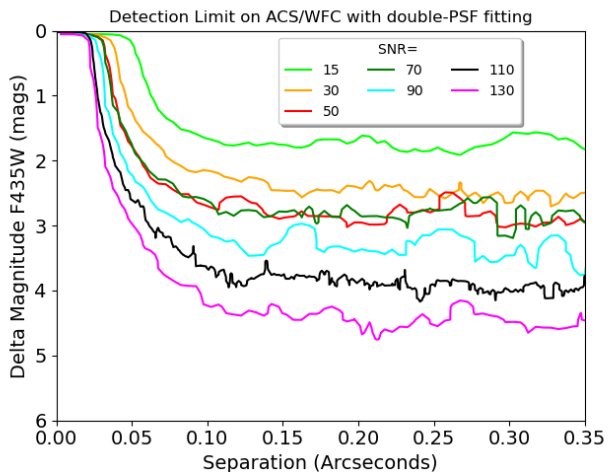

Figure 1. Each line shows the 0.1% false positive probability line associated with our double-PSF fitting routine for the listed S/N in the F435W filter on HST/ACS, adapted from Paper II.

Our data set spans five filters within which specific sources can be imaged multiple times. Within one filter, we can combine the false positive probability values derived for the multiple images of the same source if the fitted separation, Δmag, and position angle distributions are all consistent, i.e. the code is fitting the

same feature within all images. We evaluate this by calculating the Bhattacharyya coefficient (BC) between each pair of fits which determines the similarity between two distributions. For distributions with BCs > 0.1, we classify them as consistent and multiply the corresponding false positive probabilities to arrive at a total false positive probability within one filter. For BCs < 0.1, we use the best-fit among the images to calculate the false positive probability of the fit to this source. For sources that appear in multiple filters, we calculate the BC of the separation and position angle distributions only as the Δmag is not expected to be the same across filters. We then calculate a global false positive probability by multiplying the individual probabilities of the separate filters. The resulting false positive probability is then evaluated as to whether it meets our criterion for a true binary detection ($< 0.1\%$).

In Paper II, we also show that the completeness of our search entirely overlaps the region with false positive probability $< 0.1\%$, meaning that we expect to be able to recover all companions that meet our detection criteria. The completeness was determined by constructing artificial binaries in the same way we constructed artificial singles and evaluating how well we can recover the known parameters of these binaries through the χ_ν^2 test statistic. We also compared the reliability of our false positive analysis from artificial single stars to the same process using real single stars. We showed that the 0.1% false positive probability curve is nearly identical between real and artificial singles, highlighting the accuracy of the empirical PSFs as models to real data. Refer to Paper II for a more detailed description of this entire process with figures portraying these results.

3. RESULTS

3.1. *Detections*

We made 76 detections of 44 unique companions across all filters from the sample of 276 cluster members. Twenty-one detections were made in the F435W filter, 24 in the F555W filter, 29 in the F658N filter, 2 in the F775W filter, and 0 in the F850LP filter. Three detections were made only in the F435W filter, five in only F555W, ten in only F658N, and two in only F775W. Thirteen detections were made in both the F435W and F555W filters, 13 in both the F435W and F658N filters, 14 in both the F555W and F658N filters, and 8 in the F435W, F555W, and F658N filters. Thirty of the companions were previously detected (Köhler et al. 2006; Reipurth et al. 2007; Robberto et al. 2013; Duchêne et al. 2018; De Furio et al. 2019; Strampelli et al. 2020), five of which were only detected in our Paper I. The redder filters had fewer detections due to saturation effects. The

F658N filter enabled the detection of the most companions because the narrow bandpass decreases the number of saturated sources. In Table 1, we present the photometry: the combined magnitude of the system and the difference in magnitude between the primary and companion. We constructed a color-magnitude diagram (Fig. 2) for all of the sources in our sample that were observed in the F435W and F555W filters, where both components of binary detections are shown. Figures 6 - 11 show an image of each detection made in every filter in which it was found.
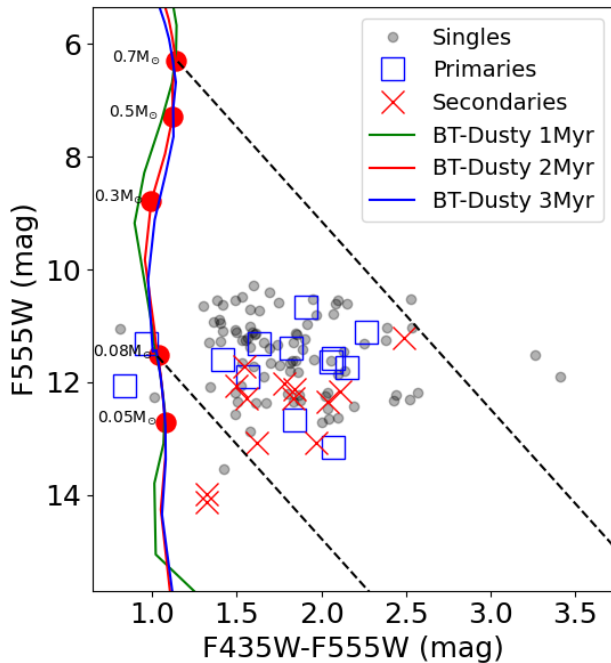

Figure 2. Color magnitude diagram for all the sources that were included in our sample with F435W and F555W data. The detected binaries are plotted with both the primary and secondary components. The solid lines are the BT-Dusty 1-3 Myr isochrones with specific masses chosen for reference. The black dashed line represent the extinction vector derived from Cardelli et al. (1989).

The estimated projected separations range from 14 - 196 au (0.034"-0.49" or 0.68 - 9.8 ACS/WFC pixels) assuming a distance of 400 pc (Großschedl et al. 2018), and mass ratios range from 0.3 - 0.97. We estimate masses using the isochrones produced from the BT-Dusty evolutionary models (Chabrier et al. 2000; Allard et al. 2001, 2011, 2012) as they have updated opacities (Barber et al. 2006). We assume a cluster age of 2 Myr, the average age of the stellar population (Reggiani et al. 2011), and the extinction to each source as derived from Da Rio et al.

(2016). They used their estimated effective temperature of each source to derive the intrinsic *(J-H)* color of the system and the observed *(J-H)* 2MASS color to estimate the extinction, assuming a 2 Myr isochrone. With these extinction values and the 2 Myr BT-Dusty isochrone, we estimate masses for the primary and companion of each binary system from the color information of Table 1, assuming the same extinction to both components. In Table 2, we present the estimated physical parameters of each binary system along with essential values from the double-PSF fitting process.

We investigated whether excess disk emission could impact the derivation of extinction for our binary detections. We took the 2MASS JHK photometry and created a color-color plot comparing to the observed colors of known pre-main sequence stars (Pecaut & Mamajek 2013). Significant disk emission would cause the observed near-IR photometry to be in excess of that expected from the photosphere, where the reddest photometry has a larger difference, causing motion toward the right in Fig. 3. With the inclusion of the reddening vector (Cardelli et al. 1989) and the classical T-Tauri locus (Meyer et al. 1997), we show that there is no large near infrared excess observed.
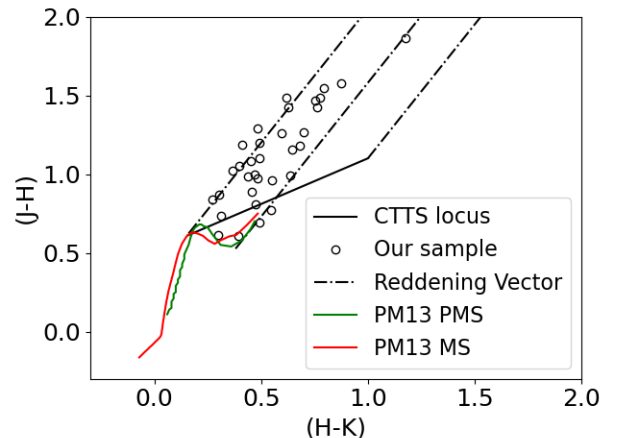

Figure 3. The J-H vs. H-K color-color plot for the sources with detected companions within our survey (black circles), showing no obvious signs of disk excess. Over-plotted are the observed pre-main sequence (PMS) and main-sequence (MS) colors of Pecaut & Mamajek (2013), PM13, the reddening vector (Cardelli et al. 1989), and the classical T-Tauri star (CTTS) locus from Meyer et al. (1997).

Because sources were found in multiple filters, we used the data from the reddest filter in which they were found to estimate masses as excess emission from accretion shocks may impact blue/UV photometry (Azevedo et al.

2006). We do not use data from the F658N (H$_\alpha$) filter to calculate masses as it will not be representative of the flux from the photosphere.

3.2. *Chance Alignments*

In order to perform a statistical analysis of our results, we must determine the probability that our candidates are not physically associated with their primaries, i.e. chance alignments. This can occur from foreground stars, background stars, and other cluster members along the line of sight. In Paper II, we used the photometric list of Robberto et al. (2013) to derive the stellar surface density as a function of radius from the cluster core that takes into account any object within the region regardless of its membership. At a distance of 115" from the cluster core (as defined by distance from Theta 1 Ori C), the stellar surface density is 0.0034 stars/arcseconds^2 for the F435W and F555W filters, beyond which a vast majority of our sources for which we can estimate masses appear. We expect to have 0.74 chance alignments give this stellar surface density, a search radius of 0.5", and 276 sources in total.

3.3. *Companion Population Analysis*

In Papers I & II, we estimated the companion frequency of low-mass stars in the ONC by defining the region of mass ratio and projected orbital separation space over which we were complete for companions for most of our sample (a = 30 - 160 au and q = 0.6 - 1.0, and a = 20 - 200 au and q = 0.5 - 1.0, respectively), see Fig. 4.

To construct this sub-sample, we defined the detection limit for each source given the 0.1% false positive probability curves associated with their S/N, e.g. Fig. 1. At each separation, there is an associated achievable contrast. This contrast value is converted into a companion mass using the 2 Myr BT-Dusty isochrones, as described in Sec. 3.1, and the minimum mass ratio that can be detected at each separation. For sources that appear in multiple filters, we assign the mass ratio limit based on the lowest achievable mass ratio between filters. We then sum over mass ratios and orbital separations to construct a combined detection probability of the entire sample, see Fig. 4, where each value of mass ratio and orbital separation has a corresponding fraction of the sample over which we are complete to companions. In our frequentist approach of Paper I & II, we took this map and determined the mass ratio and

separation range where we could detect companions to a vast majority of our sample in order to perform our statistical analyses. In this paper, we use a Bayesian approach in order to preserve all information of the survey, and do not lose information in terms of sensitivity or true detections at close separations or low mass ratio.
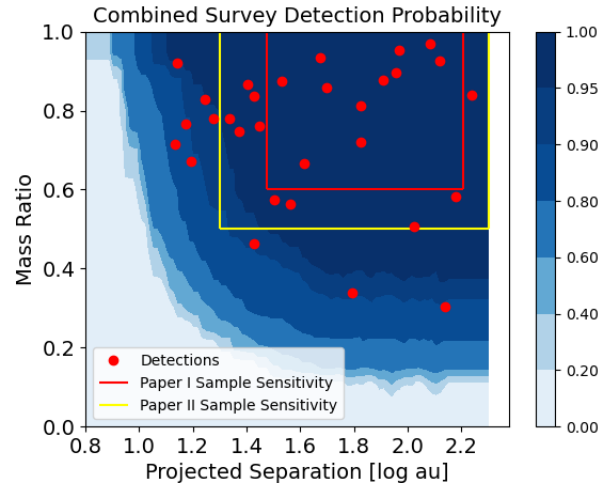

Figure 4. Summed detection probabilities for all the 245 sources in our survey in which we can calculate masses. Red circles show the projected separation and estimated mass ratios for all detected companions. Red and yellow lines show the detection limits from our past surveys in Paper I and II, respectively. We use this map in Sec. 3.3 to model the separation and mass ratio distribution of the companion population in the ONC.

We carry out a Bayesian analysis similar to the approach of Fontanive et al. (2018, 2019) to fit models of the companion population to our data without the known biases of fitting binned histogram data (e.g. Allen 2007; Kraus et al. 2011; Kraus & Hillenbrand 2012). Bayes' theorem

$$P(\theta|D) \propto P(D|\theta)P(\theta) \tag{1}$$

is based on the concept that we can evaluate the likelihood function, P(D|θ), given the observed data (D) and some initial model distribution or prior, P(θ), which then informs the model (θ) and produces a posterior distribution P(θ|D) giving the probability that the model reproduces the data. From the posterior distribution, we can then derive the values of the model parameters that best fit the data with their associated errors as this gives a probability density function (PDF) for each variable of the model.

Table 1. We list the observed magnitude information of each binary system. In each set of two columns, we present the total magnitude of each system and the difference in magnitude between the primary and companion. These values are the weighted mean calculated from all exposures of the target where the error is the 68% confidence interval. We use these values to estimate masses in Table 2. Typically, values are not listed due to saturation or low S/N in the particular filter, see Sec. 2.3. For example, sources unsaturated in the long exposures of F435W or F555W are typically saturated in those of F775W as the peak of their flux occurs at bluer wavelengths.

Source #	Total Mag (F435W)	Δ mag (F435W)	Total Mag (F555W)	Δ mag (F555W)	Total Mag (F658N)	Δ mag (F658N)	Total Mag (F775W)	Δ mag (F775W)
(1)	(2)	(3)	(4)	(5)	(6)	(7)	(8)	(9)
1	-	-	-	-	16.96 ± 0.01	1.1 ± 0.1	-	-
2	19.49 ± 0.01	0.57 ± 0.15	-	-	15.97 ± 0.01	0.46 ± 0.15	-	-
3	-	-	-	-	15.39 ± 0.01	0.04 ± 0.04	-	-
4	-	-	-	-	15.84 ± 0.01	0.20 ± 0.02	-	-
5	21.32 ± 0.02	0.38 ± 0.15	19.18 ± 0.01	0.42 ± 0.04	-	-	-	-
6	-	-	20.79 ± 0.01	0.51 ± 0.3	-	-	-	-
7	-	-	-	-	16.32 ± 0.01	0.25 ± 0.02	-	-
8	20.51 ± 0.02	2.88 ± 0.04	18.63 ± 0.01	3.46 ± 0.01	15.99 ± 0.01	2.58 ± 0.02	-	-
9	-	-	-	-	14.91 ± 0.01	1.10 ± 0.01	-	-
10	20.60 ± 0.01	1.22 ± 0.03	19.42 ± 0.01	0.22 ± 0.02	-	-	-	-
11	-	-	18.61 ± 0.01	0.77 ± 0.15	16.46 ± 0.02	0.8 ± 0.15	-	-
12	-	-	21.56 ± 0.03	0.3 ± 0.2	18.20 ± 0.02	0.61 ± 0.09	-	-
13	20.56 ± 0.01	0.9 ± 0.3	18.96 ± 0.01	0.95 ± 0.3	-	-	-	-
14	-	-	20.45 ± 0.01	0.2 ± 0.2	-	-	-	-
15	22.00 ± 0.02	0.54 ± 0.06	20.11 ± 0.02	0.41 ± 0.02	17.67 ± 0.02	0.52 ± 0.03	-	-
16	-	-	-	-	14.65 ± 0.01	1.56 ± 0.01	-	-
17	-	-	-	-	15.44 ± 0.01	1.84 ± 0.02	-	-
18	21.06 ± 0.01	0.30 ± 0.14	19.08 ± 0.01	0.5 ± 0.2	16.46 ± 0.02	0.4 ± 0.2	-	-
19	19.15 ± 0.01	0.01 ± 0.01	-	-	15.33 ± 0.01	0.22 ± 0.01	-	-
20	-	-	21.74 ± 0.05	0.48 ± 0.08	-	-	-	-
21	-	-	-	-	15.62 ± 0.01	0.04 ± 0.02	-	-
22	19.92 ± 0.01	0.99 ± 0.09	18.76 ± 0.01	0.41 ± 0.03	-	-	-	-
23	19.81 ± 0.01	0.43 ± 0.04	-	-	-	-	-	-
24	-	-	19.48 ± 0.02	1.54 ± 0.15	16.53 ± 0.02	1.7 ± 0.3	-	-
25	-	-	20.36 ± 0.01	0.87 ± 0.03	17.91 ± 0.04	0.8 ± 0.15	-	-
26	20.98 ± 0.01	1.46 ± 0.11	19.20 ± 0.01	1.66 ± 0.05	16.71 ± 0.02	1.27 ± 0.07	-	-
27	20.89 ± 0.01	0.34 ± 0.02	19.22 ± 0.01	0.12 ± 0.02	16.83 ± 0.02	0.42 ± 0.02	-	-
28	19.63 ± 0.02	0.23 ± 0.02	-	-	-	-	-	-
29	20.79 ± 0.01	0.33 ± 0.03	18.43 ± 0.01	0.10 ± 0.01	16.40 ± 0.01	0.28 ± 0.02	-	-
30	-	-	20.45 ± 0.01	2.2 ± 0.1	-	-	-	-
31	18.64 ± 0.01	1.43 ± 0.01	-	-	-	-	-	-
32	18.87 ± 0.01	2.23 ± 0.02	-	-	15.45 ± 0.01	1.79 ± 0.02	-	-
33	19.17 ± 0.01	0.19 ± 0.02	-	-	15.49 ± 0.02	0.17 ± 0.02	-	-
34	-	-	22.12 ± 0.03	0.62 ± 0.06	-	-	-	-
35	-	-	21.36 ± 0.03	1.33 ± 0.03	18.41 ± 0.03	0.27 ± 0.04	-	-
36	-	-	-	-	-	-	19.49 ± 0.02	0.16 ± 0.02
37	19.22 ± 0.01	0.86 ± 0.02	-	-	15.34 ± 0.02	0.94 ± 0.03	-	-
38	-	-	-	-	-	-	17.61 ± 0.01	0.27 ± 0.01
39	22.53 ± 0.02	0.09 ± 0.07	20.76 ± 0.01	0.8 ± 0.2	18.11 ± 0.02	0.20 ± 0.08	-	-
40	21.24 ± 0.04	0.7 ± 0.2	19.19 ± 0.02	0.71 ± 0.03	16.92 ± 0.05	0.62 ± 0.08	-	-
41	-	-	-	-	17.08 ± 0.02	0.08 ± 0.03	-	-
42	-	-	20.51 ± 0.02	1.12 ± 0.03	17.83 ± 0.01	0.88 ± 0.04	-	-
43	20.51 ± 0.02	0.6 ± 0.2	19.06 ± 0.01	0.5 ± 0.3	-	-	-	-
44	-	-	-	-	15.45 ± 0.01	1.96 ± 0.02	-	-

M. De Furio et al.

Table 2. Candidate binaries with masses (M$_\odot$), mass ratios (q), projected separations in arcseconds, physical separation in au, and position angles in degrees. To estimate masses, we used the 2 Myr BT-Dusty isochrone and the A$_v$ estimates from Da Rio et al. (2016). We assumed a distance of 400 pc (Großschedl et al. 2018). Binary parameters are the weighted mean calculated from all exposures of the target where the error is the 68% confidence interval. We also show the S/N of the target for the filter within which it is brightest along with the χ^2_ν associated with that filter. We do not show the S/N and χ^2_ν within each filter, but they fulfill the requirements of Sec. 2.3.

Source #	2MASS ID	M$_{prim}$	M$_{sec}$	q	A$_v$	Projected Sep.	Physical Sep.	PA (deg)	χ^2_ν	S/N
		(M$_\odot$)	(M$_\odot$)		(mag)	(arcseconds)	(AU)	(E of N)		
1	J05341202-0524196	-	-	-	-	0.05 ± 0.001	20.2 ± 0.4	254.91	1.19	164
2	J05342650-0523239	0.20	0.15	0.78	1.14	0.054 ± 0.001	21.68 ± 0.4	283.21	1.37	370
3	J05342753-0528284	-	-	-	-	0.050 ± 0.002	20.0 ± 0.4	236.64	1.72	517
4	J05344083-0528095	-	-	-	-	0.210 ± 0.001	83.0 ± 0.4	45.22	1.63	350
5	J05344878-0517464	0.30	0.26	0.87	2.93	0.063 ± 0.002	25.2 ± 0.8	96.16	1.52	389
6	J05345009-0517121	0.14	0.10	0.72	2.68	0.034 ± 0.002	13.6 ± 0.8	294.44	0.92	100
7	J05345099-0517565	-	-	-	-	0.250 ± 0.001	100.0 ± 0.4	49.8	1.22	195
8	J05345120-0516549	0.78	0.24	0.30	4.7	0.346 ± 0.001	137.2 ± 0.4	91.09	1.52	554
9	J05345265-0529452	-	-	-	-	0.398 ± 0.001	159.0 ± 0.4	176.86	1.00	670
10	J05345483-0525125	0.14	0.12	0.88	1.48	0.202 ± 0.001	80.8 ± 0.4	323.6	1.18	250
11	J05345683-0521363	0.81	0.63	0.78	5.16	0.048 ± 0.002	19.0 ± 0.6	101.49	1.27	414
12	J05350121-0521444	0.10	0.084	0.84	3.03	0.067 ± 0.003	27 ± 1	283.57	0.91	38
13	J05350160-0524101	0.09	0.06	0.67	0.0	0.042 ± 0.003	16 ± 1	196.84	1.42	307
14	J05350161-0533380	0.64	0.59	0.92	6.47	0.035 ± 0.003	14 ± 1	52.59	0.93	190
15	J05350207-0518226	0.28	0.24	0.86	3.66	0.125 ± 0.001	49.8 ± 0.3	107.5	1.22	148
16	J05350243-0520465	-	-	-	-	0.350 ± 0.001	140.2 ± 0.4	118.82	1.53	605
17	J05350274-0519444	-	-	-	-	0.292 ± 0.001	116.8 ± 0.4	241.55	1.07	301
18	J05350309-0522378	0.32	0.26	0.83	2.93	0.044 ± 0.002	17.5 ± 0.8	46.22	0.99	255
19	J05350476-0517421	-	-	-	-	0.270 ± 0.001	110.0 ± 0.2	196.11	0.97	373
20	J05350617-0522124	0.36	0.30	0.84	5.99	0.43 ± 0.005	172 ± 2	185.79	0.70	37
21	J05350642-0527048	-	-	-	-	0.177 ± 0.001	70.8 ± 0.4	148.61	1.37	264
22	J05350739-0525481	0.13	0.10	0.76	0.56	0.070 ± 0.001	28.0 ± 0.4	240.08	0.75	238
23	J05350985-0519339	0.79	0.69	0.87	5.29	0.085 ± 0.001	34.0 ± 0.4	325.1	1.35	163
24	J05351021-0523215	1.20	0.69	0.57	6.87	0.080 ± 0.005	32 ± 2	200.74	0.98	153
25	J05351188-0521032	-	-	-	-	0.440 ± 0.005	176 ± 2	110.15	0.98	84
26	J05351227-0520452	0.55	0.31	0.56	4.39	0.093 ± 0.002	37.2 ± 0.8	113.23	1.16	166
27	J05351270-0527106	0.20	0.19	0.95	2.1	0.233 ± 0.001	93.2 ± 0.2	230.86	0.99	265
28	J05351365-0528462	0.66	0.61	0.92	4.64	0.329 ± 0.001	131.5 ± 0.2	62.82	1.15	314
29	J05351445-0517254	0.50	0.49	0.98	3.85	0.297 ± 0.001	118.6 ± 0.4	255.47	1.45	664
30	J05351475-0534167	1.02	0.47	0.46	7.34	0.067 ± 0.003	27 ± 1	143.29	0.97	193
31	J05351491-0536391	0.40	0.24	0.58	1.88	0.387 ± 0.001	150.6 ± 0.4	73.38	1.50	690
32	J05351534-0519021	0.18	0.062	0.34	0.0	0.157 ± 0.001	63.0 ± 0.4	252.44	1.68	400
33	J05351547-0527227	0.59	0.55	0.94	3.87	0.117 ± 0.001	47.0 ± 0.4	218.2	1.69	366
34	J05351624-0528337	0.42	0.34	0.81	6.76	0.167 ± 0.003	67 ± 1	355.36	0.87	25
35	J05351676-0517167	0.13	0.064	0.51	2.86	0.265 ± 0.002	105.8 ± 0.8	118.05	0.97	75
36	J05351789-0518352	-	-	-	-	0.280 ± 0.001	111.8 ± 0.4	99.38	1.27	211
37	J05351794-0525338	0.36	0.26	0.72	2.26	0.167 ± 0.003	67 ± 1	332.53	0.65	213
38	J05351884-0522229	0.04	0.03	0.9	0.0	0.226 ± 0.001	90.6 ± 0.4	124.72	1.25	449
39	J05351986-0531038	0.65	0.49	0.75	6.64	0.061 ± 0.001	24.2 ± 0.4	168.32	1.04	162
40	J05352017-0523085	-	-	-	-	0.232 ± 0.005	93 ± 2	194.32	0.74	215
41	J05352032-0536394	-	-	-	-	0.099 ± 0.001	39.6 ± 0.2	324.78	1.68	179
42	J05352190-0515011	0.36	0.24	0.67	4.52	0.103 ± 0.001	41.4 ± 0.4	90.65	1.06	166
43	J05352534-0525295	0.16	0.12	0.77	1.24	0.035 ± 0.003	14 ± 1	89.78	1.02	203
44	J05352543-0521515	-	-	-	-	0.489 ± 0.001	195.6 ± 0.2	64.46	1.48	242

We assume simple functional forms for the mass ratio and projected orbital separations distributions guided by previous work. We define the mass ratio distribution as a power-law:

$$\frac{dN_1}{dq} \propto \begin{cases} q^{\beta} & \text{if } \beta \geq 0 \\ (1-q)^{-\beta} & \text{if } \beta < 0 \end{cases} \quad (2)$$

where β is the power-law index, and the piecewise function ensures symmetry about q=0.5 as defined in Fontanive et al. (2019). We define the projected orbital separation distribution as a log-normal:

$$\frac{dN_2}{da} = \frac{1}{\sqrt{2\sigma_{loga}^2}} e^{-\frac{(log(a)-log(a_o))^2}{2\sigma_{loga}^2}} \quad (3)$$

where $log(a_o)$ is the mean and σ_{loga} is the standard deviation of the distribution.

We use the python module PyMultiNest (Buchner et al. 2014) that performs the Nested Sampling Monte Carlo analysis using MultiNest (Feroz et al. 2009) to adequately sample our parameter space and estimate the best fitting model to our observations. Importantly, PyMultiNest also calculates the evidence of the model tested by integrating eq. 1 over all parameters which can then be used to compare different models. Nested sampling is based on generating a user-defined large number of live points that are sampled directly from the prior distribution with their likelihoods evaluated and sorted. Then, points are sampled again from the priors until a point reaches a likelihood greater than the lowest likelihood of the original set of live points. This process continues to maximize the likelihood until the effect of sampling becomes negligible. Buchner et al. (2014) describe this as a "scan vertically from the least probable zones to the most probable".

We define our likelihood function used in the sampling routine based on Poisson statistics and the physical parameters of our detected companions (Fontanive et al. 2018). First, the Poisson likelihood is calculated with:

$$\mathcal{L}_p = \frac{k^d e^{-k}}{d!} \quad (4)$$

where k (mean of the Poisson distribution) is the expected number of companion detections given the model and d is the number of detections observed in the data. We evaluate the expected number of detections with

$$k = \sum_{i=1}^{n} p_i * CF * \frac{N}{n} \quad (5)$$

where CF is the companion frequency of the sample (mean number of companions per primary star) over all

mass ratios and 10-200 au (our survey sensitivity in projected separation), N is the total number of sources in our sample (here, 245), n is the number of generated companions in the sampling process, and p_i is the probability that the i generated companion will be detected given our survey sensitivity. We assign p_i based on the physical parameters of the generated companions and the probability that they would be detected in our survey, see Fig. 4. A companion generated with q = 0.01 and log(a) = 1.0 would result in p_i = 0.0, but a companion with q = 1.0 and log(a) = 1.8 would result in p_i = 1.0.

Each time we evaluate the likelihood of a model, we sample the prior distribution for β, $log(a_o)$, σ_{loga}, and CF. For our case, we do not have informed priors on the free parameters, so we generate flat distributions with -5.0 < β < 5.0, 0.0 < $log(a_o)$ < 4.0, 0.1 < σ_{loga} < 5.0, and 0.0 < CF < 1.0. Priors for $log(a_o)$ and σ_{loga} are log-flat, so that each au is equally weighted. Then, we generate the mass ratio and projected orbital separation distributions of eqs. 2 and 3 based on those sampled values. From each model, we generate n = 10^4 companions, with mass ratios = 0 - 1 and projected orbital separations = 10 - 200 au, and determine the detection probability p_i for each based on Fig. 4. We sum over all n generated companions to derive the expected number of detections k, and then compute the Poisson likelihood where CF is a free parameter.

We then calculate the total likelihood given the information from the model and our real detections. As done in Fontanive et al. (2018), we use the sampled parameters to generate the model. We then multiply the model by the combined survey detection probability in mass ratio and projected orbital separation space. This produces a joint distribution that gives the expected companion distribution based on the sensitivity of the survey. Then, we calculate the joint probability of each true detection from our survey given that sampled model distribution and our detection limits, p_j. The total likelihood is then calculated as:

$$\mathcal{L} = \mathcal{L}_p * \prod_{j=1}^{d} p_j \quad (6)$$

We use our list of detected multiple systems with estimated primary masses of 0.08-0.7 $M_\odot$ (24 in total) to represent the low-mass stellar population as the companion properties can depend on primary mass. Stars with masses > 0.7 $M_\odot$ were only observable in F435W or F555W due to their high extinctions, typically A_v > 5 mag.

From our sample of 24 low-mass binaries in the ONC, we estimated the following four parameters over all mass

ratios and projected orbital separation 10-200 au with
1σ errors (68% confidence interval): $\beta = 2.01^{+0.99}_{-0.80}$, CF
$= 0.13^{+0.04}_{-0.03}$, $\log(a_o) = 1.71^{+1.47}_{-2.17}$, and $\sigma_{loga} = 3.03^{+1.32}_{-1.42}$.
As shown in Fig. 5, the parameters of the projected
orbital separation distribution are unconstrained, likely
due to our sensitivity between 10 - 200 au (only 1.3
orders of magnitude). Unless the distribution was very
narrow, this search radius limited our ability to fit a
log-normal distribution to the detected companions.

We then re-ran our fitting code to model the separa-
tion distribution as a power-law with index β_a, follow-
ing eq. 2. We estimated the following three parameters
with 1σ errors: $\beta = 2.08^{+1.03}_{-0.85}$, $CF = 0.13^{+0.05}_{-0.03}$, $\beta_a =$
$0.19^{+0.31}_{-0.31}$, see Fig. 5. The estimated mass ratio power
law index and companion frequency were consistent be-
tween both models.

One of the useful features of nested sampling is cal-
culating the Bayesian evidence of a particular model to
which other models can be compared. The log-evidence
of the four parameter model is -177.1 while the log-
evidence of the three parameter model is -177.8. Trotta
(2008) show that when comparing two models a differ-
ence in the log-Bayesian evidence < 1 is inconclusive and
therefore no distinction can be drawn between the two
models.

4. DISCUSSION

Many studies in the Galactic field and in star-forming
regions have characterized their companion population
and estimated the companion frequency as a function
of primary mass. We can compare our results to other
surveys in order to search for differences as a function
of primary mass and star-forming environment which
could inform our understanding of multiple formation
and evolution.

4.1. Comparison to the Galactic Field
4.1.1. Mass Ratio Distribution

Reggiani & Meyer (2013) analyzed two Galactic field
multiplicity surveys to characterize the mass ratio distri-
butions of solar-type (Raghavan et al. 2010) and M-type
(Janson et al. 2012) stars. They found the distributions
of mass ratios between the two surveys consistent, and
therefore combined the data and fit a power-law using
the maximum-likelihood estimation of Feigelson & Babu
(2012), resulting in $\beta = 0.25 \pm 0.29$. Using the results of
our 3-parameter model, we see a 2.0σ difference between
our fitted power-law exponent and that of Reggiani &
Meyer (2013).

The sample of primary stars in the Janson et al. (2012)
survey to which they detected companions had a signif-
icant portion of masses > 0.3 $M_\odot$. A significant portion

of the sources in our sample however have a mass < 0.3
$M_\odot$, see Fig. 2, potentially indicative of a difference
in the mass ratio distribution of mid-late M-stars and
early M-stars. Offner et al. (2022) performed a similar
analysis as Reggiani & Meyer (2013) where they fit a
power-law to the mass ratio distribution of the results
from the Winters et al. (2019) field M-star survey. For
primary masses 0.3 - 0.6 $M_\odot$, they find a power-law in-
dex of 0.1 ± 0.4, also a 2.1σ difference compared to our
model. However, they also found a power-law index of
0.7 ± 0.5 for primary masses 0.15 - 0.3 $M_\odot$ (more similar
to our sample, a difference of 1.4σ)

We can also compare our results to the brown dwarf
multiplicity study of Fontanive et al. (2018) who found
a power law index of $6.1^{+4.0}_{-2.7}$ to their companion popu-
lation. This results in a 1.7σ difference compared to our
survey.

4.1.2. Companion Frequency

In our survey, we were also able to constrain the com-
panion frequency of our sample over mass ratios = 0 - 1
and projected separations 10 - 200 au. We can compare
these results to those of Susemiehl & Meyer (2022) who
constrain the orbital separation distribution and com-
panion frequency of M-stars in the Galactic field using a
combination of multiple surveys that extend to primary
masses of 0.13 $M_\odot$, more similar to our sample see Fig.
2. We take eqs. 2 and 3 to define a new equation to
characterize the companion frequency of a survey given
the detection limits:

$$CF = C_n * \int_{q_1}^{q_2} \frac{dN_1}{dq} \int_{a_1}^{a_2} \frac{dN_2}{da} \qquad (7)$$

where C_n is an integration coefficient and CF is the
companion frequency.

Susemiehl & Meyer (2022) model the semi-major axis
distribution as a log-normal resulting in a peak $\log(a_o) =$
$1.68^{+0.14}_{-0.16}$ and $\sigma_{loga} = 0.97 \pm 0.19$, having corrected pro-
jected separations to physical separations using a mul-
tiplicative factor of 1.26 (Fischer & Marcy 1992). They
estimate the companion frequency over $0.6 \leq q \leq 1.0$
and $0 \leq a \leq 10,000$ au assuming the mass ratio distri-
bution from Reggiani & Meyer (2013), resulting in CF=
0.229 ± 0.028. Taking those bounds as the bounds of the
integrals in eq. 7, we can solve for the constant C_n. We
then integrate over the bounds of our own results ($0.0 \leq$
$q \leq 1.0$ and $12.6 \leq a \leq 252$ au after converting to phys-
ical separations with their same multiplicative factor)
and arrive at an expected companion frequency of the
Galactic field over the sensitivity of our survey. We re-
peated this process 10^4 times, sampling the companion
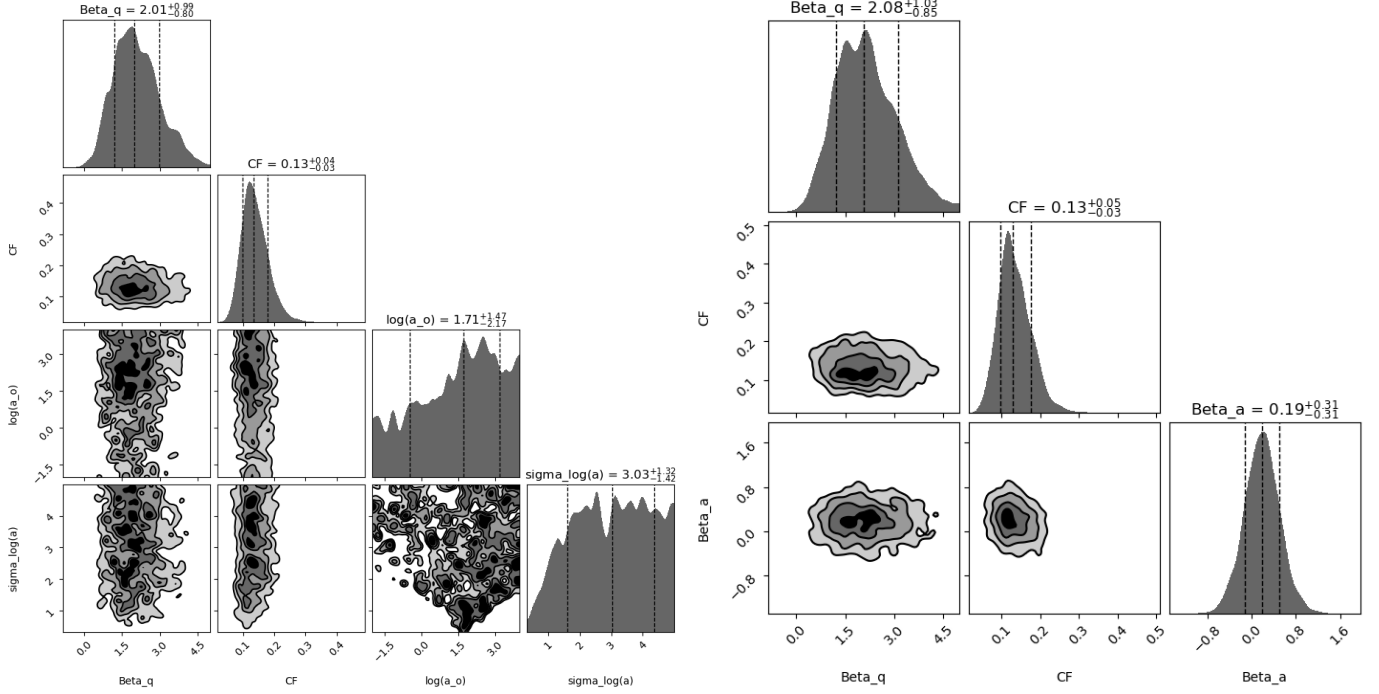parameters given their errors from Reggiani & Meyer

Figure 5. Corner plots representing the posterior distributions of the four and three parameter models used in our fit to the companion population. Beta_q is the exponent to the power law model of the mass ratio distribution, CF is the companion frequency over q=0-1 and a=10-200 au, log(a_o) is the mean of the log-normal separation distribution used in the four parameter model, sigma_log(a) is the standard deviation of the log-normal separation distribution used in the four parameter model, and Beta_a is the power law exponent to the separation distribution used in the three parameter model. The separation distribution is unconstrained with a log-normal, likely due to the limited range of our survey. Evidence values show no statistical preference between the 3 and 4 parameter model, and therefore we use the three parameter model fits for further analysis.

(2013) and Susemiehl & Meyer (2022), evaluating the expected companion frequency each time. We estimate a companion frequency of $0.244^{+0.076}_{-0.053}$ over mass ratios 0-1.0 and semi-major axes 12.6-252 au, 1.5σ difference compared to our estimate in the ONC.

4.2. Comparison to Taurus

Kraus et al. (2011) performed a multiplicity survey in Taurus, sensitive to companions between 3-5000 au. In order to directly compare our results to their companion population, we must restrict their sample of primary stars over a similar mass range and restrict the companion detections over a common separation and mass ratio to which our survey and theirs is sensitive. Therefore, we restricted their sample to sources with primary masses ≤ 0.45 M$_\odot$, where the mean primary mass of the sample is 0.31 M$_\odot$ compared to 0.29 M$_\odot$ in our ONC sample. Our Bayesian analysis evaluates the companion frequency over all mass ratios and projected separations = 10-200 au. Of the 34 stars in their sample with masses < 0.45 M$_\odot$, 12 had companions between projected separations of 10-200 au. To determine how this compares

to our survey, we converted these results to a binomial distribution following the formalism of Burgasser et al. (2003). Then, we sampled the results of our companion frequency distribution and integrated the binomial distribution of the results of Kraus et al. (2011) from 0 to the sampled ONC companion frequency to determine the posterior probability that our ONC results resemble the observed Taurus results. Taking the mean of all the samples, we arrive at a probability of 0.002 that our ONC model can describe the Taurus observations.

4.3. Implications

Our analysis of the companion population of low-mass M-stars in the ONC identified 44 companions and constrained the mass ratio distribution with a power law fit with exponent $\beta = 2.08^{+1.03}_{-0.85}$ and a companion frequency $= 0.13^{+0.05}_{-0.03}$ over 10-200 au and q=0-1. Due to our limited sensitivity in separation, we could not place meaningful constraints on the separation distribution.

We identified a 2σ difference between the power-law exponent of the mass ratio distribution for stars with masses ≥ 0.3 M$_\odot$ in the Galactic field from the stud-

ies of Reggiani & Meyer (2013) and Offner et al. (2022) and the results of our Bayesian analysis in the ONC for primary stars down to the hydrogen burning limit. Importantly, we find a 1.4σ difference between the mass ratio distribution of our results and those of Offner et al. (2022) for primary mass 0.15-0.3 $M_\odot$ and a 1.7σ difference compared to the results of Fontanive et al. (2018) for brown dwarf primaries (likely due to their large errors).

Kraus & Hillenbrand (2012) searched for companions at separations = 7 - 5000 au to stars with masses 0.07 - 0.5 $M_\odot$ in Taurus and Upper Sco, and found a trend in the mass ratio distribution similar to the field where $\beta = 0.18^{+0.33}_{-0.3}$ for 0.3 - 0.5 $M_\odot$ primaries and $\beta = 1.02^{+0.59}_{-0.52}$ for 0.15 - 0.3 $M_\odot$ primaries. Although these results are over a wider range of separations, the mass ratio distribution appears consistent with the Galactic field population for the same primary masses and also consistent with our results in the ONC for lower mass primaries (1σ difference). These results are potentially indicative of a primordial mass ratio distribution that is an outcome of the star formation process and mostly unaffected by dynamical interactions (Parker & Reggiani 2013), over the separations sampled.

Previous studies have identified preferential circumbinary disk accretion onto the companion as a mechanism to drive mass ratios toward unity (Young & Clarke 2015; Satsuka et al. 2017). These companions can be produced through turbulent fragmentation or disk fragmentation, and can migrate inward through interactions with the circumstellar disk or gas from the natal cloud, producing separation like those seen in our survey (Bate et al. 2002, 2003; Offner et al. 2010). Bate (2012) simulated a turbulent molecular cloud using a radiation hydrodynamical simulation, and found the distribution of mass ratios to stars with masses 0.1-0.5 $M_\odot$ weighted towards equal masses with 63% of these multiple systems with q > 0.6, and only 50% for stars > 0.5 $M_\odot$. These processes may be applicable to our observations within the ONC as we see a mass ratio distribution weighted towards equal masses for low-mass primaries.

In addition, we do not find a difference between the companion frequency of the ONC and that of the Galactic field (Susemiehl & Meyer 2022) for low-mass stars over q=0-1.0 and semi-major axes = 12.6-252 au. However, we find a probability of 0.002 that the companion frequency of the ONC can describe the observations of the low-mass T-association Taurus-Auriga.

High stellar density has been linked to lower companion frequency due to increased dynamical interactions that can disrupt a multiple system (Kroupa 1995b; Kroupa et al. 2001). The ONC is a high density star-

forming region, n $\sim 10^{3.5-4.5}$ stars pc^{-3} (Hillenbrand & Hartmann 1998; Marks & Kroupa 2012), that is thought to have experienced a cool-collapse phase which temporarily increases the density by roughly a factor of 10 followed by relaxation and expansion (Allison et al. 2009, 2010; Parker et al. 2011). Within temporary states of higher density, dynamical interactions become significant over 10-200 au and could have disrupted many stellar multiple systems resulting in the present day configuration of the companion population differing from the initial state. Based on the present day density of the ONC, most stellar multiple systems with separations of 10-200 au are not expected to disrupted in many 10s of Myr (Weinberg et al. 1987; De Furio et al. 2022).

Taurus-Auriga, is a low-mass, T-association, that has a low stellar density of 1-10 stars pc^{-3} (Marks & Kroupa 2012; King et al. 2012; Parker 2014). This region is not expected to have had a period of intense dynamical interactions, leaving the present day companion population likely very similar to the initial population. Additionally, the current state of the low-mass star companion population with separations $\lesssim$ 200 au will remain unchanged in the future, in excess of the Galactic field population.

Higher density regions like Westerlund 1 (10^5 $M_\odot$ pc^{-3}) and Arches ($10^{5.5}$ $M_\odot$ pc^{-3}, Clark et al. 2005), would experience an even higher level of dynamical processing, likely destroying many multiple systems with separations between 10-200 au. All types of star-forming regions will contribute to the Galactic field population, potentially with an equal number of stars over order of magnitude bins in total cluster stellar mass (Gieles 2009). If the star-forming regions within the same stellar mass bin experienced roughly equal density states, it is possible that regions that do not experience very high density states (like Taurus) will contribute an excess of companions, ONC-like clusters will contribute a comparable number of companions, and even higher density regions like Arches will contribute a paucity of companions relative to the Galactic field population over these orbital separations. In this case, the ONC would be representative of a companion population averaged over all star-forming regions commensurate with the Galactic field population.

For a more thorough analysis on the role of environment and primary mass on the formation and evolution of companion populations, we require wide-field imaging programs in diverse star-forming environments that are sensitive to members across a wide range of primary masses. The *James Webb Space Telescope (JWST)* is capable of wide-field, diffraction-limited imaging comparable to HST in the near and thermal infrared. GTO

programs 1190, 1202, 1229, and 1256 will all have NIR-Cam or NIRISS imaging data in star-forming regions of various environments, NGC 2024, NGC 1333, IC 348, and the ONC respectively. Our HST Cycle 30 program (GO-17141) is designed to perform a similar analysis as this paper (for primary masses 0.01-1.0 $M_\odot$) in NGC 1333, a moderate density star-forming region, and is well complemented by the overlapping JWST NIRISS program 1202. The data from these programs will allow us to probe similar separations as this paper, and directly compare the demographics of the companion populations within regions of different densities and evolutionary states. The up-the-ramp readout of infrared detectors on *JWST* will also drastically reduce saturation effects like those seen on ACS/WFC. These programs will also provide broad wavelength coverage in multiple filters, where the sensitivity in the infrared is also conducive to detecting members at the low-mass end of the initial mass function as well as very low mass ratios.

5. CONCLUSION

We performed a multiplicity survey of low-mass stars in the ONC using a double-PSF fitting routine with empirical PSFs with archival *HST/ACS* data. This work expanded on our previous study by using all data available in five ACS filters, updating the analysis routine to be sensitive to fainter/closer companions, and applying a Bayesian analysis to our observations to characterize the companion population. To summarize the results of our survey:

1) We detected 44 companions down to separations of 0.034" out of the 276 members in our sample, many of which were found in multiple filters. Thirty of the 44 were previously detected in other multiplicity surveys, five of which came exclusively from De Furio et al. (2019).

2) Using a Bayesian approach, we estimate the companion frequency as $0.13^{+0.05}_{-0.03}$ for low-mass stars in the ONC and the exponent of the power law to the mass ra-

tio distribution as $2.08^{+1.03}_{-0.85}$ over projected separations of 10-200 au and all mass ratios.

3) We find a 1.4σ difference in the mass ratio distribution power law exponent derived for low-mass stars in the ONC ($2.08^{+1.03}_{-0.85}$) compared to low-mass primaries (0.15 - 0.3 $M_\odot$) in the field (0.7 ± 0.5), a result consistent with that identified for low-mass primaries in Taurus and Upper Sco ($1.02^{+0.59}_{-0.52}$, Kraus & Hillenbrand 2012). These results are supportive of the hypothesis that the mass ratio distribution is mostly unaffected by dynamical processes and is the result of the star formation process itself (Parker & Reggiani 2013), cf. companion frequency.

4) We find that the companion frequency of low-mass stars in the Galactic field is consistent with that of the ONC. However, we find a significant excess in Taurus relative to the ONC, with a probability of 0.002 that the companion frequency of the ONC can describe the observations in Taurus.

5) Our findings suggest that early dynamical processing of multiple systems in high density star-forming regions is important in sculpting the companion frequency, and that the ONC may be a more representative star-forming region that will contribute to the Galactic field.

REFERENCES

Adams, F. C., Ruden, S. P., & Shu, F. H. 1989, ApJ, 347, 959, doi: 10.1086/168187

Allard, F., Hauschildt, P. H., Alexander, D. R., Tamanai, A., & Schweitzer, A. 2001, ApJ, 556, 357, doi: 10.1086/321547

Allard, F., Homeier, D., & Freytag, B. 2011, in Astronomical Society of the Pacific Conference Series, Vol. 448, 16th Cambridge Workshop on Cool Stars, Stellar Systems, and the Sun, ed. C. Johns-Krull, M. K. Browning, & A. A. West, 91. https://arxiv.org/abs/1011.5405

Allard, F., Homeier, D., Freytag, B., & Sharp, C. M. 2012, in EAS Publications Series, Vol. 57, EAS Publications Series, ed. C. Reylé, C. Charbonnel, & M. Schultheis, 3–43, doi: 10.1051/eas/1257001

Allen, P. R. 2007, ApJ, 668, 492, doi: 10.1086/521207

Allison, R. J., Goodwin, S. P., Parker, R. J., et al. 2009, ApJL, 700, L99, doi: 10.1088/0004-637X/700/2/L99

Allison, R. J., Goodwin, S. P., Parker, R. J., Portegies Zwart, S. F., & de Grijs, R. 2010, MNRAS, 407, 1098, doi: 10.1111/j.1365-2966.2010.16939.x

Anderson, J., & King, I. R. 2006, Instrument Science Report ACS 2006-01, 34 pages

Azevedo, R., Calvet, N., Hartmann, L., et al. 2006, A&A, 456, 225, doi: 10.1051/0004-6361:20054315

Barber, R. J., Tennyson, J., Harris, G. J., & Tolchenov, R. N. 2006, MNRAS, 368, 1087, doi: 10.1111/j.1365-2966.2006.10184.x

Bate, M. R. 2000, MNRAS, 314, 33, doi: 10.1046/j.1365-8711.2000.03333.x

—. 2012, MNRAS, 419, 3115, doi: 10.1111/j.1365-2966.2011.19955.x

Bate, M. R., & Bonnell, I. A. 1997, MNRAS, 285, 33, doi: 10.1093/mnras/285.1.33

Bate, M. R., Bonnell, I. A., & Bromm, V. 2002, MNRAS, 336, 705, doi: 10.1046/j.1365-8711.2002.05775.x

—. 2003, MNRAS, 339, 577, doi: 10.1046/j.1365-8711.2003.06210.x

Bonnell, I. A., & Bate, M. R. 1994, MNRAS, 269, doi: 10.1093/mnras/269.1.L45

Brandner, W., Alcala, J. M., Kunkel, M., Moneti, A., & Zinnecker, H. 1996, A&A, 307, 121

Buchner, J., Georgakakis, A., Nandra, K., et al. 2014, A&A, 564, A125, doi: 10.1051/0004-6361/201322971

Burgasser, A. J., Kirkpatrick, J. D., Reid, I. N., et al. 2003, ApJ, 586, 512, doi: 10.1086/346263

Cardelli, J. A., Clayton, G. C., & Mathis, J. S. 1989, ApJ, 345, 245, doi: 10.1086/167900

Chabrier, G., Baraffe, I., Allard, F., & Hauschildt, P. 2000, ApJ, 542, 464, doi: 10.1086/309513

Clark, J. S., Negueruela, I., Crowther, P. A., & Goodwin, S. P. 2005, A&A, 434, 949, doi: 10.1051/0004-6361:20042413

Da Rio, N., Tan, J. C., Covey, K. R., et al. 2016, ApJ, 818, 59, doi: 10.3847/0004-637X/818/1/59

De Furio, M., Meyer, M. R., Reiter, M., et al. 2022, ApJ, 925, 112, doi: 10.3847/1538-4357/ac36d4

De Furio, M., Reiter, M., Meyer, M. R., et al. 2019, ApJ, 886, 95, doi: 10.3847/1538-4357/ab4ae3

Duchêne, G., & Kraus, A. 2013, ARA&A, 51, 269, doi: 10.1146/annurev-astro-081710-102602

Duchêne, G., Lacour, S., Moraux, E., Goodwin, S., & Bouvier, J. 2018, MNRAS, 478, 1825, doi: 10.1093/mnras/sty1180

Feigelson, E. D., & Babu, G. J. 2012, Modern Statistical Methods for Astronomy

Feroz, F., Hobson, M. P., & Bridges, M. 2009, MNRAS, 398, 1601, doi: 10.1111/j.1365-2966.2009.14548.x

Fischer, D. A., & Marcy, G. W. 1992, ApJ, 396, 178, doi: 10.1086/171708

Fontanive, C., Biller, B., Bonavita, M., & Allers, K. 2018, MNRAS, 479, 2702, doi: 10.1093/mnras/sty1682

Fontanive, C., Rice, K., Bonavita, M., et al. 2019, MNRAS, 485, 4967, doi: 10.1093/mnras/stz671

Ghez, A. M., McCarthy, D. W., Patience, J. L., & Beck, T. L. 1997, ApJ, 481, 378, doi: 10.1086/304031

Ghez, A. M., Neugebauer, G., & Matthews, K. 1993, AJ, 106, 2005, doi: 10.1086/116782

Gieles, M. 2009, MNRAS, 394, 2113, doi: 10.1111/j.1365-2966.2009.14473.x

Goodwin, S. P., Whitworth, A. P., & Ward-Thompson, D. 2004, A&A, 414, 633, doi: 10.1051/0004-6361:20031594

Großschedl, J. E., Alves, J., Meingast, S., & Hasenberger, B. 2018, arXiv e-prints. https://arxiv.org/abs/1812.08024

Hillenbrand, L. A., & Hartmann, L. W. 1998, ApJ, 492, 540, doi: 10.1086/305076

Janson, M., Hormuth, F., Bergfors, C., et al. 2012, ApJ, 754, 44, doi: 10.1088/0004-637X/754/1/44

King, R. R., Goodwin, S. P., Parker, R. J., & Patience, J. 2012, MNRAS, 427, 2636, doi: 10.1111/j.1365-2966.2012.22108.x

Köhler, R., Petr-Gotzens, M. G., McCaughrean, M. J., et al. 2006, A&A, 458, 461, doi: 10.1051/0004-6361:20054561

Kratter, K. M., Matzner, C. D., & Krumholz, M. R. 2008, ApJ, 681, 375, doi: 10.1086/587543

Kraus, A. L., & Hillenbrand, L. A. 2012, ApJ, 757, 141, doi: 10.1088/0004-637X/757/2/141

Kraus, A. L., Ireland, M. J., Martinache, F., & Hillenbrand, L. A. 2011, ApJ, 731, 8, doi: 10.1088/0004-637X/731/1/8

Kroupa, P. 1995a, MNRAS, 277, 1507, doi: 10.1093/mnras/277.4.1507

—. 1995b, MNRAS, 277, doi: 10.1093/mnras/277.4.1491

Kroupa, P., Aarseth, S., & Hurley, J. 2001, MNRAS, 321, 699, doi: 10.1046/j.1365-8711.2001.04050.x

Leinert, C., Zinnecker, H., Weitzel, N., et al. 1993, A&A, 278, 129

Luhman, K. L., Mamajek, E. E., Allen, P. R., & Cruz, K. L. 2009, ApJ, 703, 399, doi: 10.1088/0004-637X/703/1/399

Marks, M., & Kroupa, P. 2012, A&A, 543, A8, doi: 10.1051/0004-6361/201118231

Mazeh, T., Goldberg, D., Duquennoy, A., & Mayor, M. 1992, ApJ, 401, 265, doi: 10.1086/172058

Meyer, M. R., Calvet, N., & Hillenbrand, L. A. 1997, AJ, 114, 288, doi: 10.1086/118474

Offner, S. S. R., Kratter, K. M., Matzner, C. D., Krumholz, M. R., & Klein, R. I. 2010, ApJ, 725, 1485, doi: 10.1088/0004-637X/725/2/1485

Offner, S. S. R., Moe, M., Kratter, K. M., et al. 2022, arXiv e-prints, arXiv:2203.10066. https://arxiv.org/abs/2203.10066

Parker, R. J. 2014, MNRAS, 445, 4037, doi: 10.1093/mnras/stu2054

Parker, R. J., Goodwin, S. P., & Allison, R. J. 2011, MNRAS, 418, 2565, doi: 10.1111/j.1365-2966.2011.19646.x

Parker, R. J., & Reggiani, M. M. 2013, MNRAS, 432, 2378, doi: 10.1093/mnras/stt600

Pecaut, M. J., & Mamajek, E. E. 2013, ApJS, 208, 9, doi: 10.1088/0067-0049/208/1/9

Press, W. H., Teukolsky, S. A., Vetterling, W. T., & Flannery, B. P. 2007, Numerical recipes 3rd edition: The art of scientific computing (Cambridge university press)

Raghavan, D., McAlister, H. A., Henry, T. J., et al. 2010, ApJS, 190, 1, doi: 10.1088/0067-0049/190/1/1

Reggiani, M., & Meyer, M. R. 2013, A&A, 553, A124, doi: 10.1051/0004-6361/201321631

Reggiani, M., Robberto, M., Da Rio, N., et al. 2011, A&A, 534, A83, doi: 10.1051/0004-6361/201116946

Reid, I. N., Lewitus, E., Allen, P. R., Cruz, K. L., & Burgasser, A. J. 2006, AJ, 132, 891, doi: 10.1086/505626

Reipurth, B., Guimarães, M. M., Connelley, M. S., & Bally, J. 2007, AJ, 134, 2272, doi: 10.1086/523596

Reipurth, B., & Zinnecker, H. 1993, A&A, 278, 81

Robberto, M., Soderblom, D. R., Bergeron, E., et al. 2013, ApJS, 207, 10, doi: 10.1088/0067-0049/207/1/10

Satsuka, T., Tsuribe, T., Tanaka, S., & Nagamine, K. 2017, MNRAS, 465, 986, doi: 10.1093/mnras/stw2709

Simon, M., Ghez, A. M., Leinert, C., et al. 1995, ApJ, 443, 625, doi: 10.1086/175554

Strampelli, G. M., Aguilar, J., Pueyo, L., et al. 2020, ApJ, 896, 81, doi: 10.3847/1538-4357/ab8eb3

Susemiehl, N., & Meyer, M. R. 2022, A&A, 657, A48, doi: 10.1051/0004-6361/202038582

Trotta, R. 2008, Contemporary Physics, 49, 71, doi: 10.1080/00107510802066753

Weinberg, M. D., Shapiro, S. L., & Wasserman, I. 1987, ApJ, 312, 367, doi: 10.1086/164883

Winters, J. G., Henry, T. J., Jao, W.-C., et al. 2019, AJ, 157, 216, doi: 10.3847/1538-3881/ab05dc

Young, M. D., & Clarke, C. J. 2015, MNRAS, 452, 3085, doi: 10.1093/mnras/stv1512
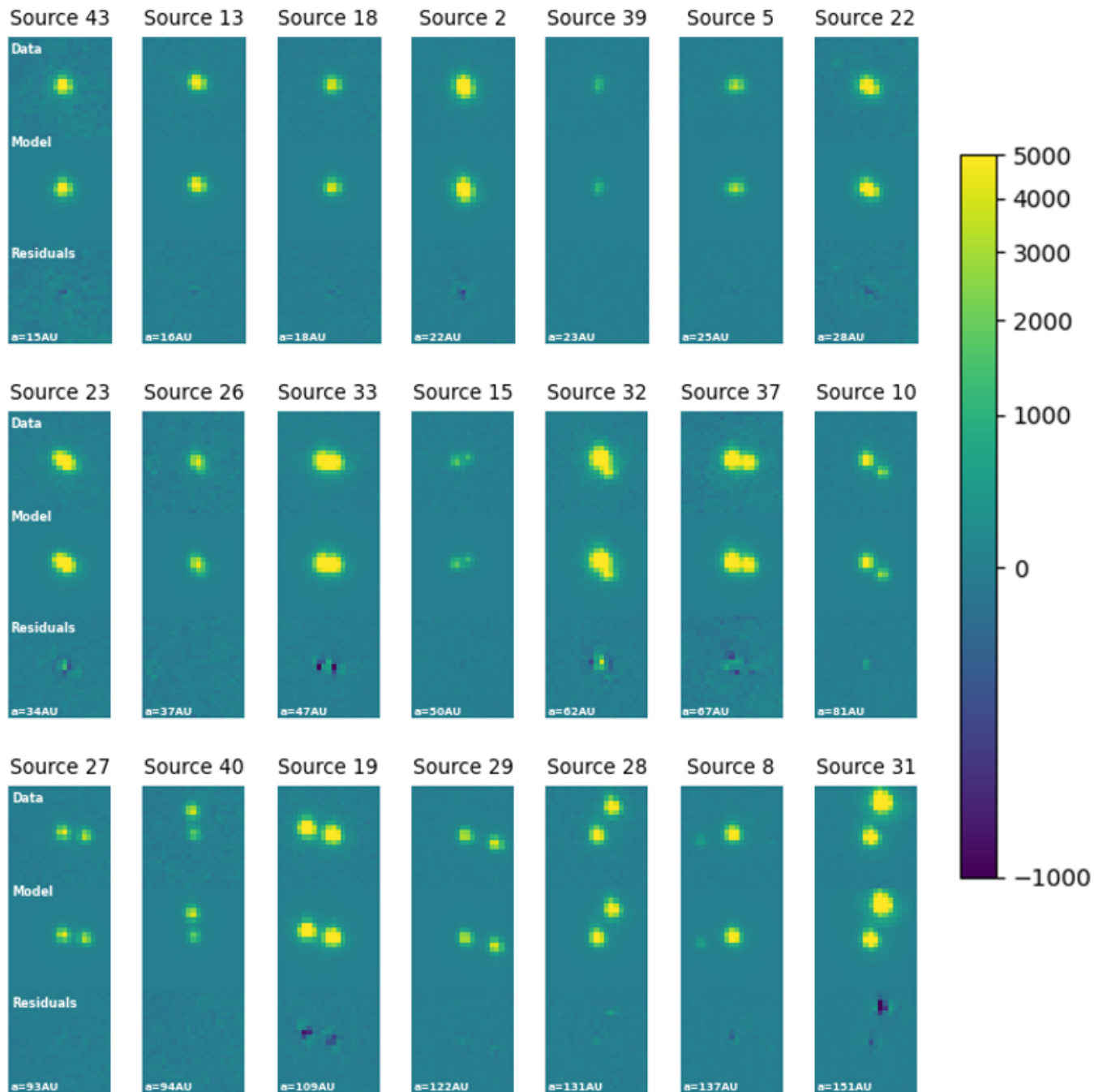
Figure 6. We display all the binary detections made in the F435W filter, showing one image per detection. The top panel shows the 21x21 postage stamp cutout of the HST/ACS data, the middle panel shows our double-PSF model, and the bottom panel shows the residuals. Each binary is labeled with their Source # that corresponds to a 2MASS ID listed in Table 2 and the estimated separation is given at the bottom of each image. Sources are listed left to right and top to bottom in order of increasing orbital separation. The colorbar shows the dynamic range of all the images in units of detector counts.

Figure 7. Same as Fig. 6 but for the F555W filter.

M. De Furio et al.

Figure 8. Continuation of Fig. 7.

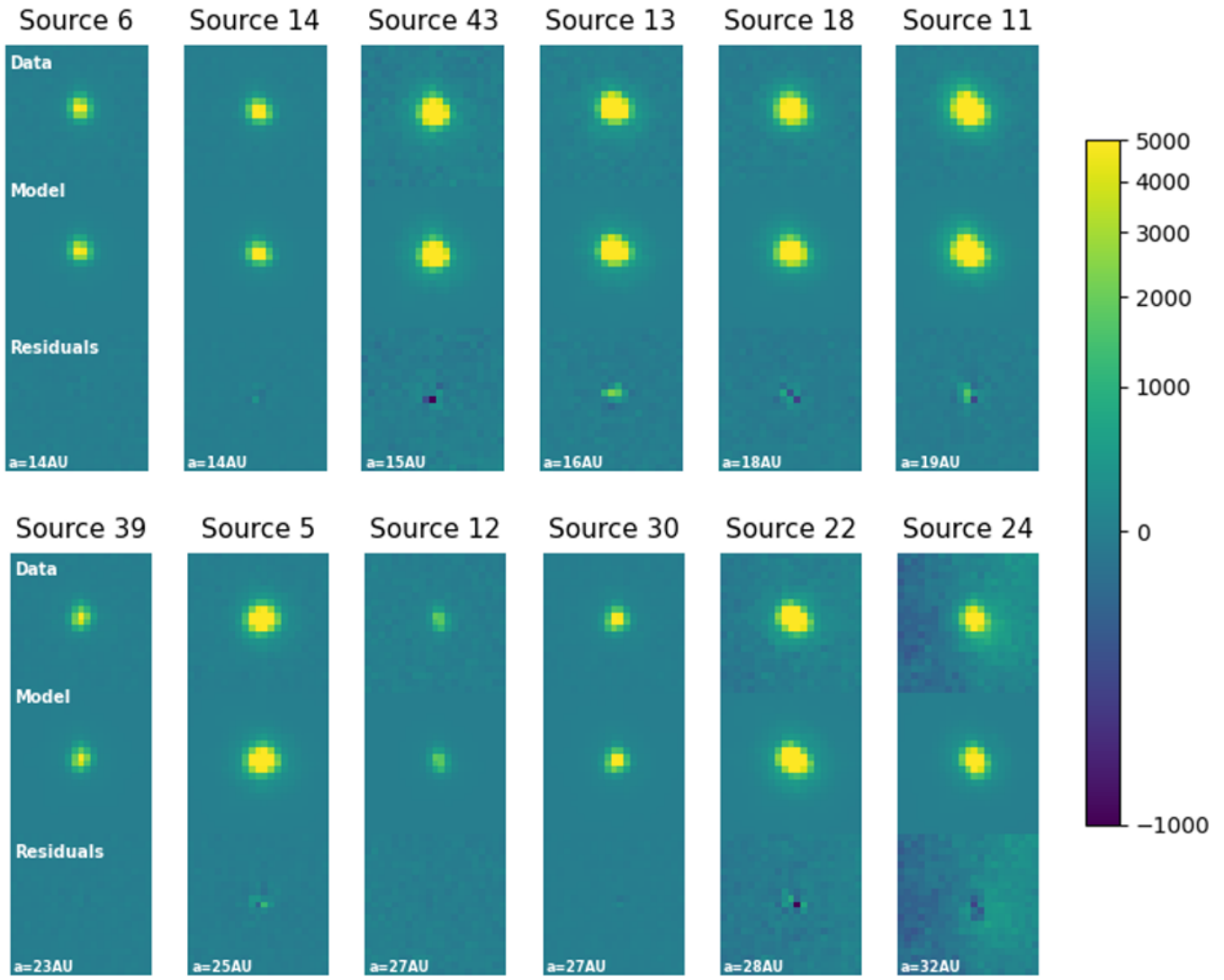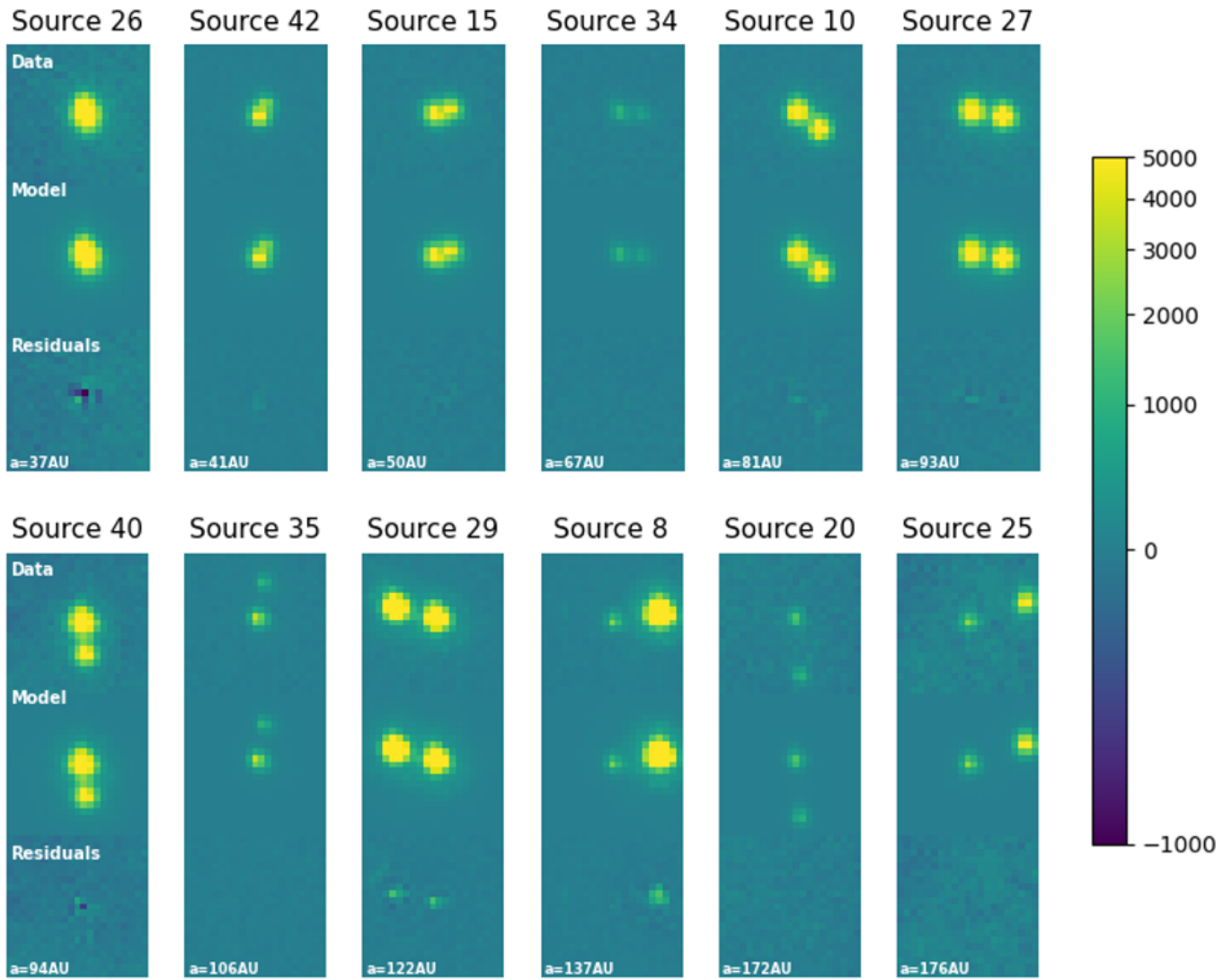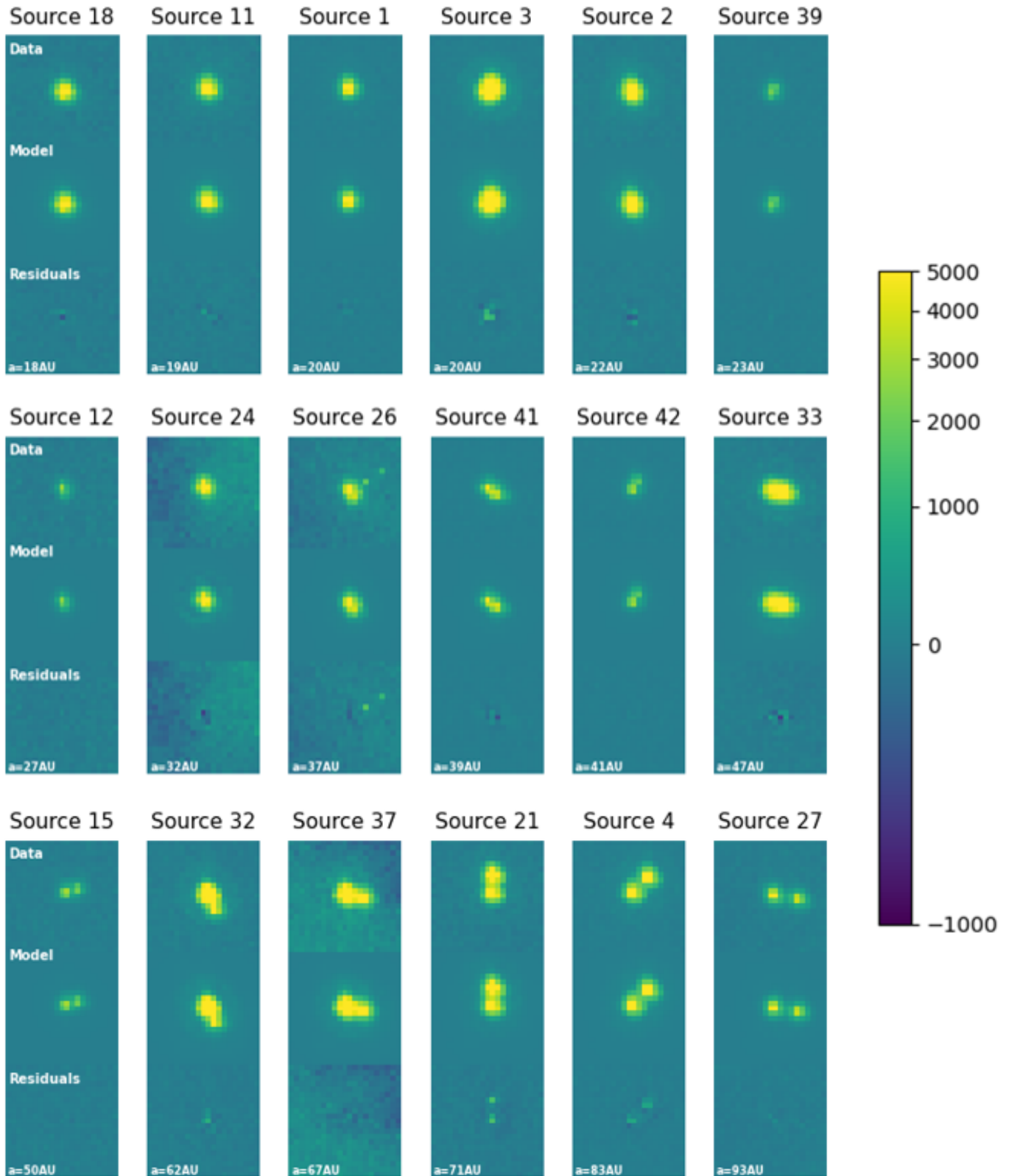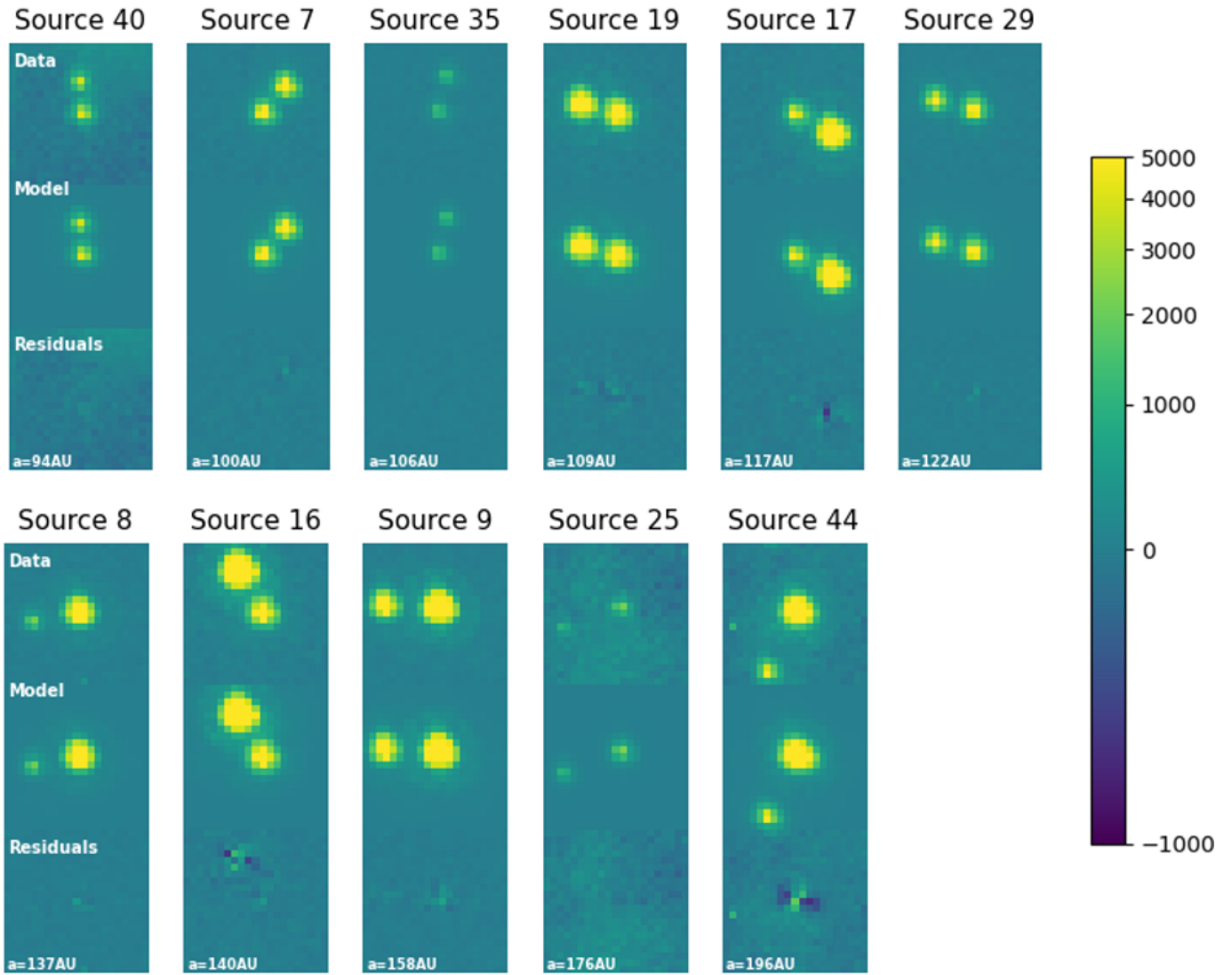**Figure 9.** Same as Fig. 6 but for the F658N filter.
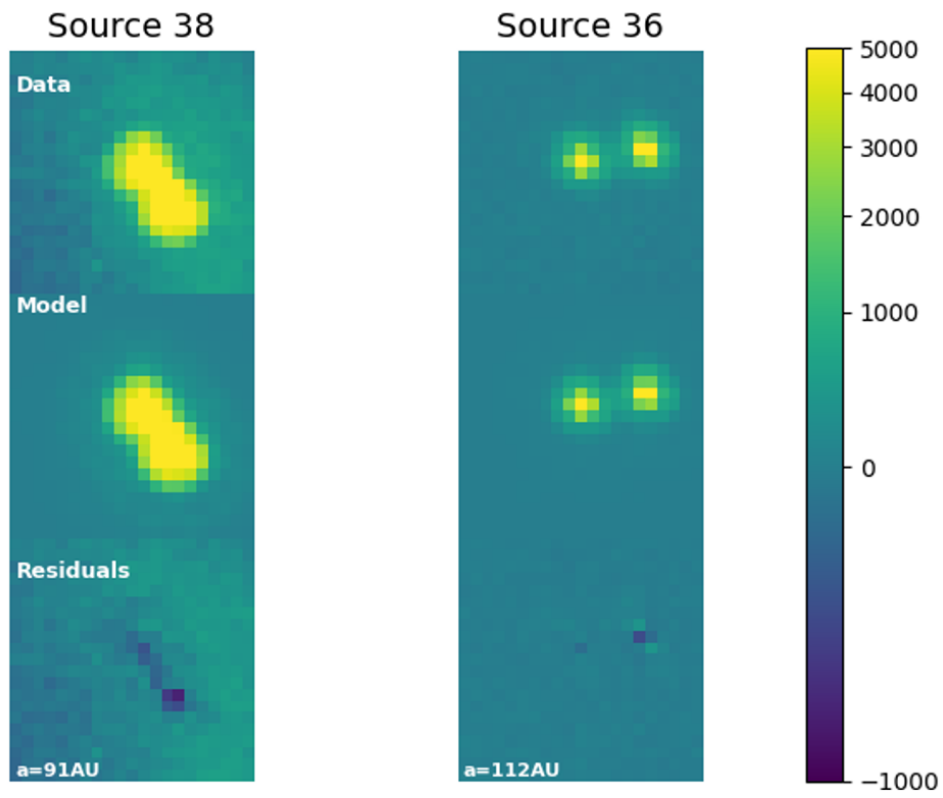
Figure 10. Continuation of Fig. 9.

Figure 11. Same as Fig. 6 but for the F775W filter.

Table 3. All sources within the sample, listed with their highest signal-to-noise (S/N) within all images of the HST Treasury Program data.

2MASSID	S/N	2MASSID	S/N	2MASSID	S/N	2MASSID	S/N
J05341202-0524196	164	J05342080-0523291	302	J05342650-0523239	370	J05342698-0518033	134
J05342753-0528284	517	J05342926-0523509	54	J05342949-0513551	506	J05342954-0523437	435
J05343168-0528269	587	J05343202-0527426	240	J05343955-0527174	133	J05344083-0528095	350
J05344184-0534299	239	J05344286-0525163	311	J05344441-0526061	341	J05344656-0523256	299
J05344677-0526048	304	J05344679-0521291	376	J05344791-0535438	315	J05344828-0532351	171
J05344877-0519073	343	J05344878-0517464	389	J05344896-0528168	321	J05344907-0526266	451
J05345009-0517121	100	J05345085-0529250	513	J05345099-0517565	195	J05345120-0516549	554
J05345201-0524187	402	J05345233-0530080	499	J05345259-0515366	215	J05345265-0529452	670
J05345275-0527545	510	J05345359-0526371	501	J05345418-0528543	580	J05345483-0525125	250
J05345555-0536061	245	J05345560-0529375	275	J05345583-0519454	65	J05345675-0526372	209
J05345683-0521363	414	J05345693-0522062	195	J05345701-0523000	256	J05345714-0533294	437
J05345737-0514334	214	J05345792-0529460	195	J05345802-0517376	327	J05345826-0538257	41
J05345827-0525332	196	J05345837-0521166	183	J05345853-0532498	231	J05345879-0521176	307
J05345893-0513455	127	J05345918-0523078	247	J05345931-0523326	182	J05350024-0518508	352
J05350101-0524103	401	J05350116-0529551	715	J05350121-0521444	38	J05350129-0520168	375
J05350133-0520221	267	J05350148-0528207	474	J05350160-0524101	307	J05350161-0533380	190
J05350201-0518341	126	J05350207-0518226	148	J05350218-0529098	487	J05350243-0520465	605
J05350270-0532249	110	J05350274-0519444	301	J05350284-0522082	106	J05350309-0522378	255
J05350315-0518299	380	J05350322-0517532	147	J05350332-0516227	606	J05350370-0522457	25
J05350396-0518597	331	J05350416-0520156	55	J05350434-0538311	183	J05350437-0523138	689
J05350450-0526044	323	J05350461-0524424	146	J05350476-0517421	373	J05350481-0522387	326
J05350487-0520574	80	J05350495-0521092	587	J05350506-0536438	638	J05350513-0520244	453
J05350537-0524105	249	J05350540-0524150	128	J05350560-0518248	161	J05350561-0529223	531
J05350571-0523540	283	J05350584-0527016	347	J05350588-0527090	138	J05350609-0514249	180
J05350615-0519556	322	J05350617-0522124	37	J05350627-0522027	213	J05350642-0527048	264
J05350727-0522266	235	J05350732-0538409	48	J05350739-0525481	238	J05350744-0526401	379
J05350768-0536587	303	J05350773-0521014	311	J05350784-0529174	670	J05350803-0536140	346
J05350822-0524032	42	J05350829-0524348	161	J05350834-0527569	325	J05350838-0528293	498
J05350859-0526194	106	J05350870-0529016	465	J05350873-0522566	60	J05350920-0530585	99
J05350959-0527599	426	J05350976-0521282	136	J05350985-0519339	163	J05351015-0527574	146
J05351021-0523215	153	J05351029-0519563	176	J05351031-0521130	223	J05351041-0519523	92
J05351047-0526003	72	J05351050-0522455	282	J05351057-0533136	295	J05351073-0526280	244
J05351083-0525569	80	J05351088-0528007	370	J05351121-0517209	498	J05351163-0522515	153

Table 4. Continuation of Table 3

2MASSID	S/N	2MASSID	S/N	2MASSID	S/N	2MASSID	S/N
J05351165-0524213	169	J05351165-0531011	340	J05351178-0521555	159	J05351185-0517259	119
J05351188-0521032	84	J05351197-0522541	156	J05351216-0530201	503	J05351227-0520452	166
J05351256-0516332	186	J05351269-0519353	82	J05351270-0527106	265	J05351277-0520349	91
J05351282-0539077	566	J05351294-0528498	243	J05351301-0519041	350	J05351303-0534035	184
J05351304-0520302	256	J05351305-0521532	41	J05351324-0527541	480	J05351330-0520189	143
J05351336-0522261	150	J05351343-0521073	295	J05351345-0517103	454	J05351348-0530481	514
J05351351-0517173	418	J05351352-0527286	391	J05351356-0527573	198	J05351357-0535080	324
J05351365-0528462	314	J05351375-0534548	325	J05351379-0519254	210	J05351382-0527368	269
J05351389-0518531	99	J05351397-0521233	69	J05351421-0520042	183	J05351444-0533190	509
J05351445-0517254	664	J05351465-0523018	138	J05351475-0534167	193	J05351491-0536391	690
J05351534-0519021	400	J05351545-0517383	368	J05351547-0527227	366	J05351548-0535118	368
J05351559-0534466	236	J05351567-0517472	82	J05351569-0528155	120	J05351571-0526283	279
J05351587-0522328	75	J05351596-0516575	269	J05351609-0524112	110	J05351624-0528337	25
J05351627-0532021	260	J05351632-0515380	357	J05351661-0519357	185	J05351676-0517167	75
J05351689-0517029	36	J05351694-0525469	338	J05351700-0515443	346	J05351712-0524585	132
J05351736-0520149	204	J05351743-0530253	528	J05351751-0517401	212	J05351778-0523155	193
J05351789-0518352	211	J05351794-0525061	58	J05351794-0525338	213	J05351795-0535157	560
J05351797-0516451	169	J05351797-0526506	88	J05351809-0515461	417	J05351820-0516340	284
J05351820-0524302	140	J05351826-0529538	382	J05351851-0520427	194	J05351858-0526248	143
J05351873-0518024	127	J05351884-0522229	449	J05351894-0520522	318	J05351921-0531030	69
J05351979-0530376	416	J05351983-0515089	374	J05351986-0530321	349	J05351986-0531038	162
J05352002-0529119	72	J05352017-0523085	215	J05352032-0536394	179	J05352041-0517144	285
J05352054-0524208	95	J05352067-0523531	147	J05352082-0521216	122	J05352099-0516375	509
J05352103-0522250	77	J05352104-0523490	38	J05352115-0518213	173	J05352162-0526576	129
J05352165-0517173	504	J05352172-0526443	255	J05352184-0522082	154	J05352190-0515011	166
J05352192-0528273	171	J05352194-0517043	363	J05352206-0528152	300	J05352228-0531168	412
J05352246-0525451	160	J05352266-0515085	96	J05352268-0516140	255	J05352279-0531372	643
J05352296-0522415	227	J05352303-0529414	435	J05352312-0513435	33	J05352317-0522283	572
J05352321-0521357	129	J05352331-0528100	183	J05352332-0521254	311	J05352349-0520016	100
J05352376-0518398	515	J05352396-0519076	366	J05352431-0528441	351	J05352433-0526003	181
J05352445-0524010	114	J05352463-0519096	493	J05352465-0522425	37	J05352488-0525101	218
J05352512-0522252	102	J05352522-0529516	419	J05352523-0533210	259	J05352534-0525295	203
J05352537-0524114	165	J05352543-0521515	241	J05352547-0521349	358	J05352547-0534028	360
J05352568-0530381	436	J05352571-0523094	377	J05352605-0521210	192	J05352615-0522570	50
J05352616-0520060	401	J05352618-0525203	99	J05352630-0527439	258	J05352640-0516124	65